

Topological Hopf-Link Semimetal

Wei Chen,¹ Hai-Zhou Lu,² and Jing-Min Hou^{3,*}

¹College of Science, Nanjing University of Aeronautics and Astronautics, Nanjing 210016, China

²Institute for Quantum Science and Technology and Department of Physics,
South University of Science and Technology of China, Shenzhen 518055, China

³School of Physics, Southeast University, Nanjing 211189, China

Topological nodal line semimetals are characterized by the crossing of the conduction and valence bands along one or more closed loops in the Brillouin zone. Usually, these loops are either isolated or touch each other at some highly symmetric points. Here, we introduce a new kind of nodal line semimetal, dubbed “topological Hopf-link semimetal”, that contains a pair of linked nodal loops. A concrete two-band model was constructed, which supports a pair of nodal lines with a double-helix structure, which can be further twisted into a Hopf link because of the periodicity of the Brillouin zone. The nodal lines are stabilized by the combined spatial inversion \mathcal{P} and time reversal \mathcal{T} symmetry; the individual \mathcal{P} and \mathcal{T} symmetries must be broken. The band exhibits nontrivial topology that each nodal loop carries a π Berry flux. Surface flat bands emerge at the open boundary and are exactly encircled by the projection of the Hopf link on the surface Brillouin zone. The experimental implementation of our model using cold atoms in optical lattices is discussed.

Introduction.—The recent discovery of topological insulators and superconductors has greatly deepened our understanding of the quantum phases of matter [1, 2]. For a gapped phase, the band topology can be well-described using topological invariants in terms of symmetries [3–6]. As the conduction and valence bands cross each other in the Brillouin zone, the system enters a semimetal phase. The topology of the gapless phase brings totally different stories, which gives rise to the concept of topological semimetals [7]. In three dimensions, the band crossing that carries nontrivial topology may occur at discrete points or along closed loops. The former case corresponds to Weyl/Dirac semimetals [8–11], whereas the latter case corresponds to topological nodal line semimetals (TNLSMs) [12]. Weyl and Dirac semimetals [13–25] have both been experimentally confirmed, which has increased research interest in topological semimetals. Now the latest member of topological semimetals, TNLSM, is waiting for experimental verifications [26]. A variety of candidates have been proposed [27–37], and recent experiments have shown promising results [37, 38].

In addition, the topological classification of TNLSMs remains incomplete [6, 26]. Unlike the topology of Weyl and Dirac semimetals, which can be well-described by a single topological invariant under proper symmetry protections, the topology of TNLSM is more subtle [26]. From a simple geometrical perspective, there are two configurations of zero dimensional nodal points, in which they are either coincident or not. In contrast, there are a variety of possible configurations for one dimensional nodal loops. They can (i) be isolated (Fig. 1(a)), (ii) touch at certain points, or (iii) be linked with each other (Fig. 1(b)). This intrinsic difference may considerably enrich the scenarios of TNLSMs. A typical example of

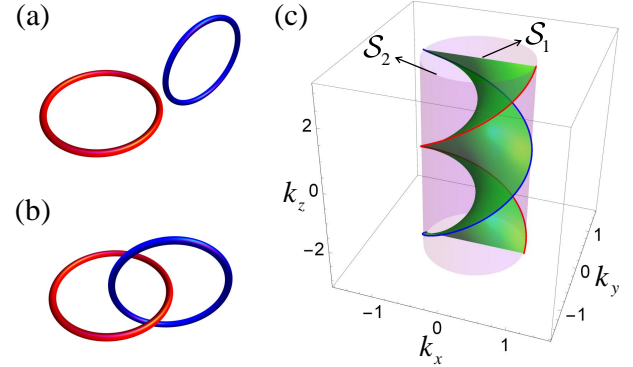


FIG. 1: (Color online). Topological configurations of two closed nodal loops: (a) isolated, or (b) forming a Hopf link. (c) Nodal lines with a double-helix structure, formed by intersecting lines of two surfaces S_1 and S_2 .

the first case is the system described by the minimal model $h(\mathbf{k}) = \sin k_z \sigma_x + [M - 4B(\sin^2 \frac{k_x}{2} + \sin^2 \frac{k_y}{2} + \sin^2 \frac{k_z}{2})] \sigma_z$, where two isolated nodal loops lie in two planes $k_z = 0, \pi$. The second case has also been reported; for instance, gyroscope-shaped nodal lines [30, 31] and the recently predicted non-symmorphic nodal chain metals [39].

In this Letter, we determined the existence of a third kind of TNLSM, in which nodal loops are linked. This novel TNLSM is denoted as a “topological Hopf-link semimetal”. In contrast to existing TNLSMs, a pair of nodal lines pass through each other and form a double-helix structure, as shown in Fig. 1(c). Because of the periodicity of the Brillouin zone, this double-helix is topologically equivalent to a Hopf link (HL), carrying a nonzero linking number. Moreover, the band also possesses nontrivial topology, in which each nodal line carries a π Berry flux, which results in novel surface states.

Two-band model with Hopf-link nodal lines.—We constructed a tight binding model based on a cubic lattice.

*Electronic address: jmhhou@seu.edu.cn

This model can be described in momentum space as follows:

$$\begin{aligned}\mathcal{H}(\mathbf{k}) &= d_x(\mathbf{k})\sigma_x - d_z(\mathbf{k})\sigma_z, \\ d_x(\mathbf{k}) &= \sin k_y \cos k_z - \sin k_x \sin k_z, \\ d_z(\mathbf{k}) &= 2 \cos k_x + 2 \cos k_y + \chi,\end{aligned}\quad (1)$$

where the Hamiltonian is chosen to be dimensionless for simplicity, the lattice constant is set to unity, $\sigma_{x,y,z}$ are the Pauli matrices for pseudospin (such as the orbital degree of freedom), and χ is a tunable parameter.

Diagonalizing the Hamiltonian produces the eigenstates $|u_{\pm}(\mathbf{k})\rangle$ of the Hamiltonian (1) of opposite energies $E_{\pm}(\mathbf{k}) = \pm\sqrt{d_x^2 + d_z^2}$. Degeneracy of the bands occurs when $d_x(\mathbf{k}) = d_z(\mathbf{k}) = 0$, which defines the nodal lines in the Brillouin zone. It can be interpreted as the intersecting lines of two surfaces $\mathcal{S}_1 : d_x(\mathbf{k}) = 0$ and $\mathcal{S}_2 : d_z(\mathbf{k}) = 0$. Here, the nodal lines form a novel double-helix structure. This becomes explicit at the limit of $k_x \ll 1, k_y \ll 1$, in which the parametric equation of \mathcal{S}_1 reduces to $k_y/k_x = \tan k_z$, which describes a helicoid, while that of \mathcal{S}_2 becomes $k_x^2 + k_y^2 = 4 + \chi \ll 1$, corresponding to a cylinder. The intersecting lines of the two surfaces pass through each other to form a double-helix, as shown in Fig. 1(c). Moreover, because of the periodicity of the Brillouin zone, the cylinder \mathcal{S}_2 folds into a torus. Correspondingly, the double-helix structure folds into an HL (Fig. 1(b)). This HL possesses a nonzero linking number, so the nodal loops cannot shrink to a point without crossing each other. In the remainder of this paper, the double-helix nodal lines are referred to as the HL for convenience.

Symmetry analysis.—In general, the nodal lines in TNLSMs are stabilized by extra symmetries imposed on the Hamiltonian [12]. This situation should also be true for the HL semimetal. For a system without spin-orbit coupling, the time reversal operator \mathcal{T} acts on the Hamiltonian through $\mathcal{T}\mathcal{H}(\mathbf{k})\mathcal{T}^{-1} = \mathcal{H}^*(-\mathbf{k})$, and the spatial inversion operator \mathcal{P} reverses the momentum as $\mathcal{P}\mathcal{H}(\mathbf{k})\mathcal{P}^{-1} = \mathcal{H}(-\mathbf{k})$. The HL semimetal phase breaks both \mathcal{T} and \mathcal{P} symmetries, as follows:

$$[\mathcal{H}, \mathcal{T}] \neq 0, [\mathcal{H}, \mathcal{P}] \neq 0. \quad (2)$$

Moreover, the HL semimetal phase does not have reflection symmetry \mathcal{R} about any plane. Thus, our scheme differs from those of existing TNLSMs, in which at least one of these three symmetries exists [27–37]. However, without individual $\mathcal{P}, \mathcal{T}, \mathcal{R}$ symmetries, the HL semimetal retains combined \mathcal{PT} symmetry [40, 41] as

$$[\mathcal{H}(\mathbf{k}), \mathcal{PT}] = \mathcal{H}(\mathbf{k}), \quad (3)$$

which reflects the reality of the Hamiltonian. In addition, the Hamiltonian (1) respects chiral symmetry, which can be described by the anticommutation relation as

$$\{\mathcal{H}(\mathbf{k}), \Gamma\} = 0, \quad (4)$$

where the chiral operator $\Gamma = i\sigma_y$ corresponds to twofold spin rotation. The Γ symmetry guarantees that the eigenstates $|u_{\pm}(\mathbf{k})\rangle$ with opposite energies always exist in pairs. Both symmetries forbid the $d_y(\mathbf{k})\sigma_y$ term to enter $\mathcal{H}(\mathbf{k})$, which is essential for the stability of the HL. The difference between these two symmetries is that the Γ symmetry simultaneously excludes the energy term $d_0(\mathbf{k})\sigma_0$ (where σ_0 is the unit matrix), whereas the \mathcal{PT} symmetry does not. As a result, the chiral symmetry not only stabilizes the HL, it also restricts its energy to zero.

Band topology and surface states.—In addition to its the novel geometric configuration, the HL also exhibits nontrivial topology. Each of the two nodal lines of the HL carries a π Berry flux in the Brillouin zone. Therefore, if one were to travel along any closed path encircling one of the nodal lines, the accumulated geometric phase would be equal to π . To demonstrate this, we first prove the stability condition for the HL, that is, the Berry curvature $\Omega(\mathbf{k})$ generically vanishes for nondegenerate points [12]. Away from the HL, the Berry curvature for the valence band can be defined as

$$\Omega_{\mu}^{-}(\mathbf{k}) = i\epsilon_{\mu\nu\lambda}\langle\partial_{\nu}u_{-}(\mathbf{k})|\partial_{\lambda}u_{-}(\mathbf{k})\rangle, \quad (5)$$

where $|u_{-}(\mathbf{k})\rangle$ is the periodic part of the Bloch wave function, ∂_{ν} denotes $\partial/\partial k_{\nu}$, and $\epsilon_{\mu\nu\lambda}$ is the Levi-Civita antisymmetric tensor. Due to the chiral symmetry (4), if $|u_{-}(\mathbf{k})\rangle$ is the wave function for the valence band, $|u_{+}(\mathbf{k})\rangle = \sigma_y|u_{-}(\mathbf{k})\rangle$ must be the eigenstate of the conduction band. A direct calculation shows that the Berry curvature of the valence band is equal to that of the conduction band for a given \mathbf{k} , $\Omega^{-}(\mathbf{k}) = \Omega^{+}(\mathbf{k})$. By using the local conservation law for the Berry curvature [42] $\Omega^{-}(\mathbf{k}) + \Omega^{+}(\mathbf{k}) = 0$, we obtain

$$\Omega^{-}(\mathbf{k}) = \Omega^{+}(\mathbf{k}) = 0. \quad (6)$$

This indicates that if a nonzero distribution of the Berry curvature exists in the Brillouin zone, it must be strictly localized along the HL. Then we may choose an arbitrary integral loop enclosing a single nodal line to calculate the Berry phase.

Without loss of generality, we can choose the integral loop of $\ell \rightarrow \mathcal{C}_1 \rightarrow \mathcal{C} \rightarrow \mathcal{C}_2$, as indicated by the arrowed lines in Fig. 2(a). This loop is composed of two line segments parallel to the y axis (ℓ and \mathcal{C}) and two segments parallel to the x axis (\mathcal{C}_1 and \mathcal{C}_2). The two x -axis paths \mathcal{C}_1 and \mathcal{C}_2 are equivalent, but oriented in opposite directions; therefore, their contributions cancel out [43]. Such a scheme benefits subsequent discussion on the surface states. We can regard k_x and k_z as parameters and derive the Berry phase of the effective one dimensional model along the y direction. The wave function of the valence band is $|u_{-}(\mathbf{k})\rangle = \left(\text{sgn}(d_x)\sqrt{\frac{1-\cos\theta}{2}}, -\sqrt{\frac{1+\cos\theta}{2}}\right)^T$, where $\cos\theta = -d_z/\sqrt{d_x^2 + d_z^2}$. The Berry phase can be ob-

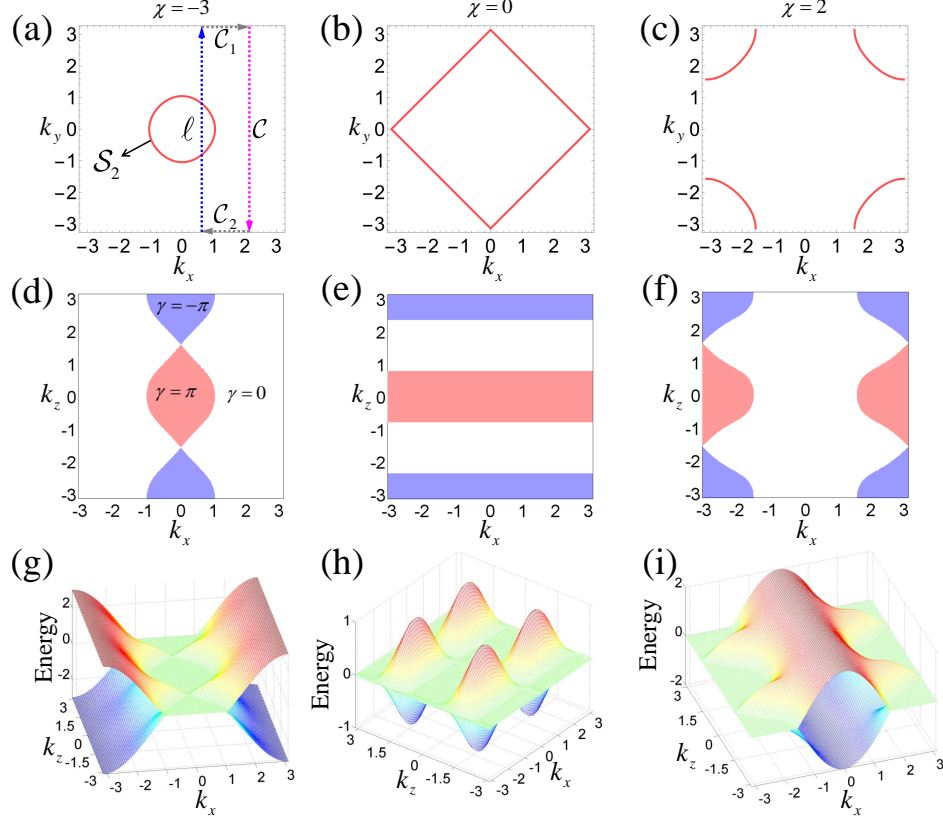


FIG. 2: (Color online). (a)-(c) Projection of the surface \mathcal{S}_2 with different values of χ (circle for $\chi < 0$, square for $\chi = 0$, and 4 open arcs for $\chi > 0$) in the $k_x - k_y$ plane. The integral paths $\ell \rightarrow \mathcal{C}_1 \rightarrow \mathcal{C} \rightarrow \mathcal{C}_2$ are indicated by the arrowed lines. (d)-(f) Berry phase distribution in the projected surface Brillouin zone as a function of k_x and k_z , with values of χ corresponding to those in (a)-(c), respectively. (g)-(i) Surface states at open boundaries in the y direction.

tained as [44]

$$\begin{aligned} \gamma &= i \int_{-\pi}^{\pi} dk_y \langle u_{-}(\mathbf{k}) | \partial_{k_y} | u_{-}(\mathbf{k}) \rangle \\ &= \frac{i}{2} \int_{-\pi}^{\pi} dk_y [\partial_{k_y} \ln \text{sgn}(d_x)] (1 - \cos \theta), \end{aligned} \quad (7)$$

in which the integral path ℓ is parallel to the y axis, as shown in Fig. 2(a). A nonzero contribution to the integral may come from the k_y -dependent sign change of $d_x(\mathbf{k})$, so the integral can be written in the neighborhood of two real roots $k_y = k_{1,2}$ of the equation $\sin k_y = \sin k_x \tan k_z$. In this case, we have $\cos \theta|_{k_y=k_{1,2}} = -\text{sgn}(d_z)$, and Eq. (7) reduces to

$$\begin{aligned} \gamma &= \frac{i}{2} \sum_{j=1,2} \int_{k_j-\delta}^{k_j+\delta} dk_y [\partial_{k_y} \ln \text{sgn}(d_x)] \\ &\quad \times [1 + \text{sgn}(2 \cos k_x + 2 \cos k_j + \chi)]. \end{aligned} \quad (8)$$

For given values of k_x and k_z , the real roots $k_{1,2}$ correspond to the crossing points of ℓ and \mathcal{S}_1 . Once ℓ passes through \mathcal{S}_1 , it contributes a π phase to the integral. Because $k_{1,2}$ must either exist as a pair or not at all, ℓ may pass through \mathcal{S}_1 either twice or never, and thus, the Berry

phase is zero if there are no additional constraints. The second factor in the integral incorporates an additional constraint, $2 \cos k_x + 2 \cos k_j + \chi > 0$, which ensures that the integral is inside \mathcal{S}_2 . Under this restriction, the path ℓ may cross \mathcal{S}_1 only once, resulting in a nontrivial Berry phase.

From this geometric viewpoint, it can be seen that the configuration of \mathcal{S}_1 and \mathcal{S}_2 determines the Berry phase distribution in the $k_x - k_z$ plane. When projected to the surface Brillouin zone, the HL defines the boundaries between the topologically trivial ($\gamma = 0$) and nontrivial ($\gamma = \pm\pi$) regions. This can be verified by the numerical results of Eq. (8), as shown in Fig. 2(a)-(f). For $\chi < 0$, \mathcal{S}_2 is a closed cylinder with a central axis located at $k_x = k_y = 0$ (Fig. 2(a)). The area with nontrivial topology is encircled by the projected HL on the surface Brillouin zone (Fig. 2(d)). Because of its double-helix structure, the neighboring nontrivial regions have opposite Berry phases. As χ increases, the area surrounded by \mathcal{S}_2 expands, as does the topologically nontrivial area. At the critical point, $\chi = 0$, the surface \mathcal{S}_2 meets the Brillouin zone boundary (Fig. 2(b)). At this point, the topologically nontrivial area reaches its maximum, which occupies half of the Brillouin zone (Fig. 2(e)). If χ in-

creases further, \mathcal{S}_2 is opened, as shown in Fig. 2(c). In this case, the area defined by $2\cos k_x + 2\cos k_y + \chi > 0$ is surrounded by both \mathcal{S}_2 and part of the Brillouin zone boundaries. For $|k_x| < \cos^{-1}(1 - \chi/2)$, there is no constraint on the interval of the integration in Eq. (8). Therefore, the Berry phase equals zero in this region, as shown in Fig. 2(f). This is equivalent to a cylinder centered at $k_x = k_y = \pi$, at which the nodal lines are confined. Considering that the topologically trivial and nontrivial regions are separated by the projection of the HL, we may choose the integral paths ℓ and \mathcal{C} , located on opposite sides of the HL, such that the integral exactly equals the π Berry flux of each nodal line. This demonstrates the nontrivial band topology of the HL semimetal phase.

The nontrivial topology of the HL suggests the existence of surface flat bands in the projected surface Brillouin zone [12]. By performing a Fourier transformation on the Bloch Hamiltonian (1) in the y direction, the energy bands with open boundaries in the y direction can be calculated. The lowest two bands are shown in Fig. 2(g-i) for different values of χ . The flat bands coincide with the regions where $\gamma = \pm\pi$, suggesting that these zero modes are topologically protected. We also calculated the Berry phase integral along the x direction, and its distribution was found to match the surface flat bands [45]. Because this system does not have C_4 rotational symmetry, the Berry phase distribution calculated along the x and y directions are different.

Experimental realization with cold atoms in optical lattices.—The high controllability of ultracold atoms in optical lattices makes them a suitable platform for the investigation of exotic physics [46]. Many novel techniques have been developed for use with these systems, such as laser-assisted tunneling [47], optical lattice shaking [48], Raman transition tunneling [49], atomic interferometry [50, 51], and Bragg scattering [52]. These techniques can be used to emulate physical phenomena that are difficult to realize in solid materials. Here, we present a scheme to realize and detect the topological HL semimetal using cold atoms in an optical lattice. A tight-binding Hamiltonian can be defined as

$$\begin{aligned}
H = & -t_1 \sum_i [c_i^\dagger \sigma_z c_{i+\hat{x}} + c_i^\dagger \sigma_z c_{i+\hat{y}}] + H.c. \\
& + t_2 \sum_i [e^{-\frac{\pi}{2}i} c_i^\dagger \sigma_x c_{i+\hat{y}+\hat{z}} + e^{-\frac{\pi}{2}i} c_i^\dagger \sigma_x c_{i+\hat{y}-\hat{z}}] + H.c. \\
& + t_2 \sum_i [c_i^\dagger \sigma_x c_{i+\hat{x}+\hat{z}} - c_i^\dagger \sigma_x c_{i+\hat{x}-\hat{z}}] + H.c. \\
& + \chi \sum_i c_i^\dagger \sigma_z c_i
\end{aligned} \tag{9}$$

where the lattice constant is set to unity, and $\hat{x}, \hat{y}, \hat{z}$ are

the primitive lattice vectors. The operators $c_{i,\sigma}$ are defined in the Wannier representation $w_i(\mathbf{r})$ at the lattice site i , with pseudospin $\sigma = \uparrow, \downarrow$ representing two intrinsic atomic states. The Bloch Hamiltonian (1) can be recovered by performing a Fourier transformation on Eq. (9), and setting the hopping coefficients to $t_1 = 1$, and $t_2 = 1/4$.

To achieve the Hamiltonian (9), we chose two hyperfine spin states $|1, -1\rangle$ and $|1, 0\rangle$ of ^{87}Rb as the pseudospins in our model, and constructed a spin-dependent cubic optical lattice using several lasers to trap two pseudospin atoms. The lattice potential along the z direction was sufficiently deep, such that the hopping along the z direction was negligibly weak [53]. The optical lattice shaking technique was applied to the spin-down optical lattice, which resulted in the renormalization of the hopping coefficient of the spin-down atoms with a negative sign [48]. Hence, the hopping coefficients of the spin-up and spin-down atoms in the x - y plane had opposite signs. Equal hopping strengths for both spins can be achieved by fine-tuning the depths of the two optical lattices. The Zeeman term in Eq. (9) can be constructed and tuned by applying an external magnetic field along the z direction. The diagonal spin-flip hopping in the y - z and x - z planes, as shown in the second and third lines of Eq. (9), can be achieved using two groups of Raman fields [45]. By properly designing the Raman lattices, onsite and nearest-neighbor spin-flip hopping are forbidden. The hopping-accompanying phase in the y - z plane can be achieved by tilting a pair of Raman lasers at an appropriate angle from the y axis in the y - z plane [45].

The configuration of the HL nodal lines and the attached Berry flux can be measured using an interferometric technique with high momentum resolution [50, 51]. The energy band of the surface states can be probed by Bragg spectroscopy [52].

Acknowledgments

We acknowledge helpful discussions with Y. X. Zhao, D. W. Zhang, W. Y. Deng, F. Mei and Z. Y. Xue. This work was supported by the National Natural Science Foundation of China under Grants No. 11504171 (W.C.), No. 11574127 (H.Z.L.) and No. 11274061 (J.M.H.). W.C. was also supported by the Natural Science Foundation of Jiangsu Province in China under Grant No. BK20150734. H.Z.L was also supported by the National Key R & D Program (Grant No.2016YFA0301700) and the National Thousand-Young-Talents Program.

[1] M. Z. Hasan and C. L. Kane, Rev. Mod. Phys. **82**, 3045 (2010).

[2] X. L. Qi and S. C. Zhang, Rev. Mod. Phys. **83**, 1057

- (2011).
- [3] X. L. Qi, T. L. Hughes, and S. C. Zhang, Phys. Rev. B **78**, 195424 (2008).
 - [4] A. P. Schnyder, S. Ryu, A. Furusaki, and A. W. W. Ludwig, Phys. Rev. B **78**, 195125 (2008).
 - [5] A. Kitaev, AIP Conf. Proc. **1134**, 22 (2009).
 - [6] C. K. Chiu, J. C. Y. Teo, A. P. Schnyder, and S. Ryu Rev. Mod. Phys. **88**, 035005 (2016).
 - [7] H. M. Weng, X. Dai, and Z. Fang, J. Phys. Condens. Matter **28**, 303001 (2016).
 - [8] S. Murakami, New Journal of Physics **9**, 356 (2007).
 - [9] X. Wan, A. M. Turner, A. Vishwanath, and S. Y. Savrasov, Phys. Rev. B **83**, 205101 (2011).
 - [10] Z. J. Wang, Y. Sun, X. Q. Chen, C. Franchini, G. Xu, H. Weng, X. Dai, and Z. Fang, Phys. Rev. B **85**, 195320 (2012).
 - [11] Z. J. Wang, H. M. Weng, Q. S. Wu, X. Dai, and Z. Fang, Phys. Rev. B **88**, 125427 (2013).
 - [12] A. A. Burkov, M. D. Hook, and L. Balents, Phys. Rev. B **84**, 235126 (2011).
 - [13] H. M. Weng, C. Fang, Z. Fang, B. A. Bernevig, and X. Dai, Phys. Rev. X **5**, 011029 (2015).
 - [14] S. M. Huang *et al.*, Nat. Commun. **6**, 7373 (2015).
 - [15] B. Q. Lv *et al.*, Phys. Rev. X **5**, 031013 (2015).
 - [16] S. Y. Xu *et al.*, Science **349**, 613 (2015).
 - [17] B. Q. Lv *et al.*, Nat. Phys. **11**, 724 (2015).
 - [18] X. Huang *et al.*, Phys. Rev. X **5**, 031023 (2015).
 - [19] B. Q. Lv *et al.*, Phys. Rev. Lett. **115**, 217601 (2015).
 - [20] Z. K. Liu *et al.*, Science **343**, 864 (2014).
 - [21] S. Y. Xu *et al.*, Science **347**, 294 (2015).
 - [22] J. Xiong *et al.*, Science **350**, 413 (2015).
 - [23] Z. K. Liu *et al.* Nat. Mater. **13**, 677 (2014).
 - [24] S. Borisenko *et al.* Phys. Rev. Lett. **113**, 027603 (2014).
 - [25] H. M. Yi *et al.*, Sci. Rep. **4**, 6106 (2014).
 - [26] C. Fang, H. M. Weng, X. Dai, and Z. Fang, Chin. Phys. B **25**, 117106 (2016).
 - [27] H. M. Weng *et al.*, Phys. Rev. B **92**, 045108 (2015).
 - [28] Y. Chen *et al.*, Nano Lett. **15**, 6974 (2015).
 - [29] M. Zeng *et al.*, arXiv:1504.03492
 - [30] Y. Kim, B. J. Wieder, C. L. Kane, and A. M. Rappe Phys. Rev. Lett. **115**, 036806 (2015).
 - [31] R. Yu, H. Weng, Z. Fang, X. Dai, and X. Hu, Phys. Rev. Lett. **115**, 036807 (2015).
 - [32] C. Fang, Y. Chen, H. Y. Kee, and L. Fu Phys. Rev. B **92**, 081201 (2015).
 - [33] A. Yamakage, Y. Yamakawa, Y. Tanaka, and Y. Okamoto, J. Phys. Soc. Jpn. **85**, 013708 (2016).
 - [34] L. S. Xie, L. M. Schoop, E. M. Seibel, Q. D. Gibson, W. Xie, and R. J. Cava, APL Mater. **3**, 083602 (2015).
 - [35] Y. Chan, C. Chiu, M. Chou, and A. Schnyder, Phys. Rev. B **93**, 205132 (2016).
 - [36] J. Zhao, R. Yu, H. Weng and Z. Fang, Phys. Rev. B **94**, 195104 (2016).
 - [37] G. Bian *et al.*, Nat. Commun. **7**, 10556 (2016).
 - [38] J. Hu *et al.*, Phys. Rev. Lett. **117**, 016602 (2016).
 - [39] T. Bzdušek *et al.*, Nature **538**, 75 (2016).
 - [40] Y. X. Zhao, Andreas P. Schnyder, and Z. D. Wang, Phys. Rev. Lett. **116**, 156402 (2016).
 - [41] D. W. Zhang *et al.*, Phys. Rev. A **93** 043617 (2016).
 - [42] D. Xiao, M. C. Chang, and Q. Niu, Rev. Mod. Phys. **82**, 1959 (2010).
 - [43] D. A. Abanin, T. Kitagawa, I. Bloch, and E. Demler Phys. Rev. Lett. **110**, 165304 (2013).
 - [44] S. Q. Shen, *Topological Insulators: Dirac Equation in Condensed Matters* (Springer-Verlag, Berlin Heidelberg, 2012).
 - [45] See Supplemental Material for a description of the Berry phase distribution in the k_y-k_z plane, the surface states at open boundaries in the x direction, and the experimental scheme for the realization of the topological HL semimetal phase using cold atoms in optical lattices.
 - [46] M. Lewenstein *et al.*, Adv. Phys. **56**, 243 (2007).
 - [47] H. Miyake, G. A. Siviloglou, C. J. Kennedy, W. C. Burton, and W. Ketterle, Phys. Rev. Lett. **111**, 185302 (2013).
 - [48] J. Struck *et al.*, Phys. Rev. Lett. **108**, 225304 (2012).
 - [49] Z. Wu *et al.*, Science **354**, 83 (2016).
 - [50] M. Atala *et al.*, Nat. Phys. **9**, 795 (2013).
 - [51] L. Duca *et al.*, Science **347**, 288 (2015).
 - [52] D. M. Stamper-Kurn *et al.*, Phys. Rev. Lett. **83**, 2876 (1999).
 - [53] For simplicity, we have omitted the hopping term along the z direction in Eq. (9), because the hopping coefficient is much smaller than t_1 . It is easy to verify that weak hopping along the z direction does not change the configurations or the Berry flux of the nodal lines.

I. 1. BERRY PHASE INTEGRAL IN THE x DIRECTION AND SURFACE STATES

We chose the integral path ℓ in Eq. (7) of the main text to be parallel to the x axis. Hence, the Berry phase can be calculated by

$$\begin{aligned}\gamma &= i \int_{-\pi}^{\pi} dk_x \langle u_{-}(\mathbf{k}) | \partial_{k_x} | u_{-}(\mathbf{k}) \rangle \\ &= \frac{i}{2} \int_{-\pi}^{\pi} dk_x [\partial_{k_x} \ln \text{sgn}(d_x)] (1 - \cos \theta),\end{aligned}\tag{S.1}$$

which can be further reduced as below:

$$\begin{aligned}\gamma &= \frac{i}{2} \sum_{j=1,2} \int_{k'_j-\delta}^{k'_j+\delta} dk_x [\partial_{k_x} \ln \text{sgn}(d_x)] \\ &\quad \times [1 + \text{sgn}(2 \cos k_y + 2 \cos k'_j + \chi)],\end{aligned}\tag{S.2}$$

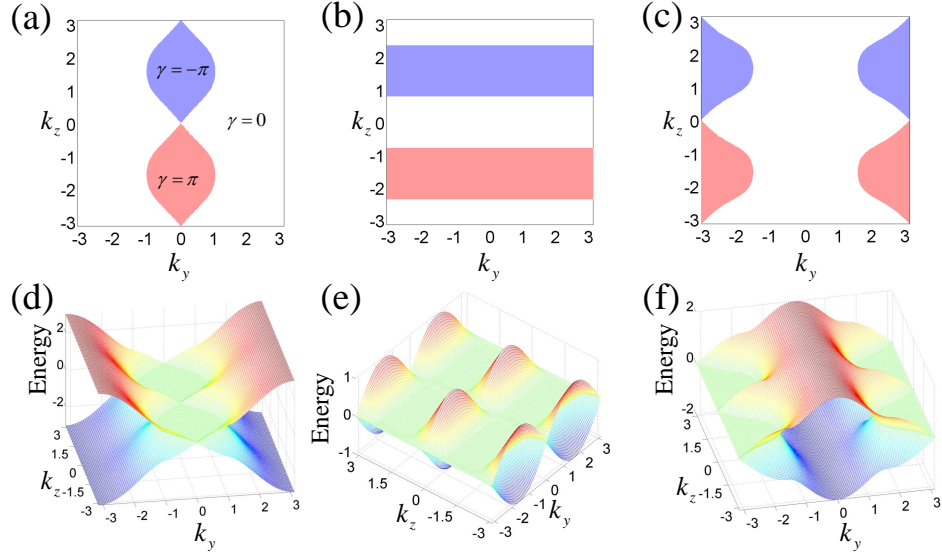


FIG. S.1: (Color). (a)-(c) Berry phase distributions in the projected surface Brillouin zone as a function of k_y and k_z , corresponding to $\chi = -3, 0$, and 2 , respectively. (d)-(f) Corresponding surface states on the open boundaries in the x direction.

where $k_x = k'_1, k'_2$ are the two real roots of the equation $\sin k_x = \sin k_y \cot k_z$. The distributions of the Berry phase in the projected surface Brillouin zone for different values of χ are shown in Fig. S.1(a)-(c). The corresponding surface states are presented in Fig. S.1(d)-(f), where the flat bands indicate the region with a nontrivial Berry phase.

II. 2. EXPERIMENTAL REALIZATION USING COLD ATOMS IN OPTICAL LATTICES

The tight-binding Hamiltonian (9) in the main text can be written as $H = H_{xy} + H_{xz} + H_{yz} + H_{Zeeman}$, with

$$\begin{aligned}
 H_{xy} &= -t_1 \sum_i [c_i^\dagger \sigma_z c_{i+\hat{x}} + c_i^\dagger \sigma_z c_{i+\hat{y}}] + H.c. \\
 H_{yz} &= t_2 \sum_i [e^{-\frac{\pi}{2}i} c_i^\dagger \sigma_x c_{i+\hat{y}+\hat{z}} + e^{-\frac{\pi}{2}i} c_i^\dagger \sigma_x c_{i+\hat{y}-\hat{z}}] + H.c. \\
 H_{xz} &= t_2 \sum_i [c_i^\dagger \sigma_x c_{i+\hat{x}+\hat{z}} - c_i^\dagger \sigma_x c_{i+\hat{x}-\hat{z}}] + H.c.. \\
 H_{Zeeman} &= \chi \sum_i c_i^\dagger \sigma_z c_i
 \end{aligned} \tag{S.3}$$

Basic experimental setup: In our model, we chose two hyperfine spin states $|1, -1\rangle$ and $|1, 0\rangle$ of ^{87}Rb as the pseudospin states $|\uparrow\rangle$ and $|\downarrow\rangle$ [1]. Cold atoms ^{87}Rb were trapped in a spin-dependent cubic optical lattice with a lattice potential of $V_\sigma(\mathbf{r}) = -V_{1,\sigma} [\cos^2(\frac{\pi x}{a_x}) + \cos^2(\frac{\pi y}{a_y})] - V_{2,\sigma} \cos^2(\frac{\pi z}{a_z})$, where $a_{x,y,z}$ are the lattice constants along the x, y, z directions, which can be constructed using several pairs of lasers.

Construction of H_{Zeeman} : The Zeeman term H_{Zeeman} can be constructed and tuned by applying an external magnetic field along the z direction, which results in an energy difference of 2χ between the spin-up and spin-down states.

Construction of H_{xy} : The lattice potential along the z direction is chosen such that it is deep enough that hopping along the z direction is negligibly weak, and thus the hopping term along the z direction can be neglected and only the nearest-neighbor hopping terms in the x - y plane are allowed. The corresponding hopping strength in the x - y plane can be written as $t_{1,\sigma} = \int d\mathbf{r} w_i^*(\mathbf{r}) [\mathbf{p}^2/(2m) + V_\sigma(\mathbf{r})] w_{i+\hat{x}(\hat{y})}(\mathbf{r})$, where $w_i(\mathbf{r})$ is a Wannier function centered at site i . The lattice shaking technique can be applied to the spin-down optical lattice, which results in the renormalization of the hopping coefficient of spin-down atoms with a negative sign, such as $t'_{1,\downarrow} = -\kappa t_{1,\downarrow}$, where κ is a positive renormalization coefficient[2]. The renormalization coefficient can be fine-tuned by properly choosing the depths of the spin dependent optical lattices, such that $t'_{1,\downarrow} = -t_{1,\uparrow} = -t_1$ in H_{xy} .

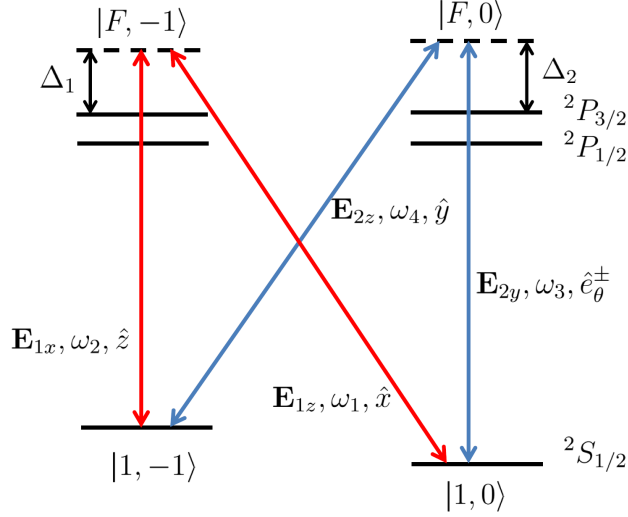


FIG. S.2: Atomic levels of ^{87}Rb and the Raman lasers used in the present study.

Construction of H_{xz} : H_{xz} describes the diagonal spin-flip hopping in the x - z plane, which can be constructed using Raman transitions, as shown in Fig.S.2. We chose the excited state $|F, -1\rangle$ as the intermediate state, which provides a Raman transition channel between the ground states $|1, -1\rangle$ and $|1, 0\rangle$ using two Raman laser fields. One of the Raman fields is a standing wave $\mathbf{E}_{1z} = \hat{x}\mathcal{E}_1 \sin(k_1 z)$ formed by a pair of oppositely propagating lasers in the z direction, with a frequency of $\omega_1 = ck_1$ (where c is the speed of light in vacuum) and exhibits linear polarization along the x axis. This field induces the transition between the $|1, 0\rangle$ and $|F, -1\rangle$ states. The other Raman laser field is a standing wave $\mathbf{E}_{1x} = \hat{z}\mathcal{E}_1 \sin(k_2 x)$ formed by a pair of oppositely propagating lasers in the x direction, with a frequency of $\omega_2 = ck_2$ and linear polarization along the z axis. This field results in the transition between states $|1, -1\rangle$ and $|F, -1\rangle$. To avoid pumping atoms to the intermediate state, the frequencies ω_1 and ω_2 were chosen to have a large detuning Δ_1 from the energy differences between the ground states and the intermediate state. The frequency difference $\delta\omega = \omega_1 - \omega_2$ was set to match the Zeeman splitting between the $|1, -1\rangle$ and $|1, 0\rangle$ states. We set $k_1 = 2\pi/a_z$ and $k_2 = 2\pi/a_x$ by fine-tuning the frequencies of the Raman lasers to ensure that the Raman lattice matches the optical lattice, as shown in Fig.S.3(a). The Raman potential, which induces spin-flip transitions, takes the form of $M_1(\mathbf{r}) = \mathcal{M}_1 \sin(2\pi x/a_x) \sin(2\pi z/a_z)$, where $\mathcal{M}_1 \propto \mathcal{E}_1^2[1]$. The profile of the Raman potential in the x - z plane is shown in Fig.S.3(a). The Raman potential has opposite signs along the two diagonal directions, such that the amplitude of the on-site spin-flip transition vanishes and the nearest-neighbor spin-flip hopping terms in the x - z plane are forbidden. However, the Raman potential induces spin-flip hopping along the diagonal directions in the x - z plane. The hopping coefficients of the two diagonal hopping terms have opposite signs, such that $t_{xz} = \int d\mathbf{r}^3 w_i^*(\mathbf{r}) M_1(\mathbf{r}) w_{i+\hat{x}+\hat{z}}(\mathbf{r}) = - \int d\mathbf{r}^3 w_i^*(\mathbf{r}) M_1(\mathbf{r}) w_{i+\hat{x}-\hat{z}}(\mathbf{r})$. $t_{xz} = t_2$ in H_{xz} can be achieved by tuning the amplitude \mathcal{E}_1 of the Raman lasers.

Construction of H_{yz} : H_{yz} describes the diagonal spin-flip hopping with an accompanying phase in the y - z plane, which can be constructed by an additional Raman transition channel via the intermediate state $|F, 0\rangle$, as shown in Fig.S.2. One of the Raman laser fields is a standing wave $\mathbf{E}_{2z} = \hat{y}\mathcal{E}_2 \sin(k_4 z)$ formed by a pair of lasers oppositely propagating in the z direction, with a frequency of $\omega_4 = ck_4$ and linear polarization along the y axis. This field induces the transition between states $|1, -1\rangle$ and $|F, 0\rangle$. The other Raman laser field is formed by two non-collinear lasers propagating in the y - z plane, with frequency $\omega_3 = ck_3$. The two lasers are described by $E_{2y}^\pm = \frac{1}{2}(\hat{z} \cos \theta \pm \hat{y} \sin \theta) \mathcal{E}_2 e^{\pm i[(k_3 y \cos \theta \mp k_3 z \sin \theta) - \pi/2]}$, where θ is the included angle between the lasers and the y axis. The two lasers form the field $E_{2y} = E_{2y}^+ + E_{2y}^- = E_{2y}^{(z)} + E_{2y}^{(y)}$, where $E_{2y}^{(z)} = \hat{z} \cos \theta \mathcal{E}_2 \sin(k_3 y \cos \theta) e^{-ik_3 z \sin \theta}$ and $E_{2y}^{(y)} = \hat{y} \sin \theta \mathcal{E}_2 \cos(k_3 y \cos \theta) e^{-i(k_3 z \sin \theta + \pi/2)}$. The laser field $E_{2y}^{(z)}$ results in the transition between states $|1, 0\rangle$ and $|F, 0\rangle$. To avoid pumping atoms to the intermediate state, the frequencies ω_3 and ω_4 were chosen to exhibit a large detuning Δ_2 from the energy differences between the ground states and the intermediate state. The Raman potential is $M_2(\mathbf{r}) = \mathcal{M}_2 \sin(k_3 y \cos \theta) \sin(k_4 z) e^{-ik_3 z \sin \theta}$, where $\mathcal{M}_2 \propto \mathcal{E}_2^2 \cos \theta[1]$. The hopping-accompanying phases can be achieved by adjusting the angle θ to satisfy the equality $k_3 \sin \theta = \pi/2a_z$. To ensure that the optical lattice matches with the Raman lattice, we set $k_3 \cos \theta = 2\pi/a_y$ by tuning the lattice constant a_y in the y direction. The difference between ω_1 and ω_4 is significantly less than ω_1 and ω_4 . There-

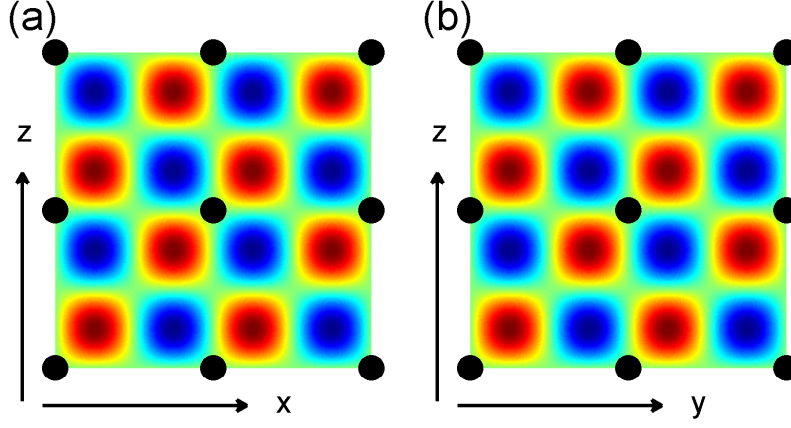


FIG. S.3: (a) Profile of the Raman potential $M_1(\mathbf{r})$ in the x - z plane. (b) Intensity of the Raman potential $M_2(\mathbf{r})$ in the y - z plane. The filled circles represent the lattice sites of the optical lattice.

fore, the difference between k_1 and k_4 can be neglected, which gives $k_4 = 2\pi/a_z$. The Raman potential can be rewritten as $M_2(\mathbf{r}) = \mathcal{M}_2 \sin(2\pi y/a_y) \sin(2\pi z/a_z) e^{-i\pi z/2a_z}$. The intensity of $M_2(\mathbf{r})$ in the y - z plane is shown in Fig.S.3(b), which indicates that the amplitude of the on-site spin-flip transition is vanishing and the nearest-neighbor spin-flip hopping terms in the y - z plane are negligible. The diagonal hopping coefficients in the y - z plane are $t_{yz}e^{-i\pi/2} = \int d\mathbf{r}^3 w_i^*(\mathbf{r}) M_2(\mathbf{r}) e^{-i\pi z/2a_z} w_{i+\hat{y}+\hat{z}}(\mathbf{r}) = \int d\mathbf{r}^3 w_i^*(\mathbf{r}) M_2(\mathbf{r}) e^{-i\pi z/2a_z} w_{i+\hat{y}-\hat{z}}(\mathbf{r})$. $t_{yz} = t_2$ in H_{yz} can be achieved by tuning the amplitude \mathcal{E}_2 of the Raman lasers.

-
- [1] Z. Wu *et al.*, Science **354**, 83 (2016).
 - [2] J. Struck *et al.*, Phys. Rev. Lett. **108**, 225304 (2012).